Sponge-like Porous Manganese(II,III) Oxide as a Highly Efficient Cathode Material for Rechargeable Magnesium Ion Batteries

Lu Wang[1], Karina Asheim[1], Per Erik Vullum[2], Ann Mari Svensson[1] and Fride Vullum-Bruer[1,*]

[1] Department of Materials Science and Engineering, NTNU, Norwegian University of Science and Technology, NO-7491 Trondheim, Norway

[2]SINTEF Materials and Chemistry, NO-7491 Trondheim, Norway

ABSTRACT: Here, we are the first to report a spinel type Mn_3O_4 as cathode material for Mg-ion battery (MIB) with graphite foil (Gif) as current collector. High coulombic efficiency and good cyclic stability of Mn_3O_4 are demonstrated, and the process is enhanced by using Mn_3O_4 nanoparticles with a sponge-like morphology. The powder exhibits a network of interconnected mesopores with well-dispersed nanoparticles (~10 nm) and large specific surface area (102 m^2 g^{-1}). This structural configuration provides easy access for electrolyte penetration which markedly enhances the utilization of electroactive material, generates high ion flux across the electrode-electrolyte interface and provides more active sites for electrochemical reactions to occur. This study can possibly open the way for exploring other similar compounds with a spinel type structure for MIB.

1. INTRODUCTION

In the last decade great efforts have been made to develop new electrochemical energy storage devices with high power and energy density, which is able to replace current Li-ion battery technology. A large part of this increased effort can be attributed to the high demand for large-scale applications, which has also triggered a closer attention to the safety and sustainability of using Li.[1-3] In particular, MIB has been regarded as the most promising candidate owing to magnesium's rich content in the Earth's crust (20,000 times more than Li), as well as its chemical stability.[4] Compared to Li, Mg is inherently much safer due to higher stability in contact with air in addition to the absence of dendritic formation during electrochemical cycling.[4,5] Also, compared to Li, Mg has a theoretical volumetric capacity of 3833 mAh cm^{-3}, nearly twice that of Li (2061 mAh cm^{-3}), indicating that MIB has a good potential for reaching a high volumetric energy density.[6,7] The elementary components of MIB are similar to Li-ion batteries and include a Mg metal anode, a cathode capable of hosting Mg, electrolyte, current collector, and separator. Among these, electrolyte and cathode materials are the two components, which so far have greatly hindered MIB to be commercialized like Li batteries.[4,5,8]

The limited selection of electrolytes which can accommodate reversible Mg deposition/stripping, offer anodic stability, provide high ionic conductivity and a wide electrochemical window, are the biggest obstacles that restrains the research and development of MIB.[9-16] So far, there are several promising electrolytes developed for MIB. For example, the well-known Mg organohaloaluminate electrolytes, $Mg(AlCl_2BuEt)_2$ complex and all-phenyl-complex (APC, $AlCl_3$-$(PhMgCl)_2$) based electrolytes, were developed by Aurbach *et al.*;[17-19] the non-corrosive *closo*- borane compounds based electrolyte and $[Mg_2(\mu\text{-}Cl)_3{\cdot}6THF](HMDSAlCl_3)$/THF electrolyte (which is chemically compatible with an electrophilic sulphur cathode) were proposed by Toyota R&D;[13,20] while the magnesium aluminum chloride complex (MACC) electrolyte without organic moiety was prepared by Doe *et al.*[12] These electrolytes possess a wide electrochemical window, high conductivity, fast kinetics of Mg deposition/dissolution, and high anodic stability that can be regarded as the milestones in the development history of MIB. However, even though these electrolytes perform remarkably well with the Mg anodes, most of them contain high concentrations of chloride anions which cause severe corrosion of most known current collectors made from metals.[2,4,21] Some typical metals (Cu, Al, Ni and stainless steel) in these electrolytes are basically anodically unstable at potentials of 2.0 V vs. Mg,[22-24] and thus result in high contact resistance between the active materials and the current collectors during electrochemical measurements. This severely affects the battery performance of the cathode materials. The strong corrosive behaviour of electrolytes developed up to now for MIB gives rise to the strict requirements for the typical metal current collectors.[3] So, to be able to study the effect of the host-structure and morphology features of the cathode on the battery performance, finding a suitable current collector with electrochemical stability over the entire potential range is extremely important.

Until now, the reported specific capacities, cycling stability and coulombic efficiencies of cathode materials for MIBs are insufficient to obtain performances comparable to that of Li-ion batteries. The major problem with cathode materials for MIB comes from the slow solid-state diffusion of Mg^{2+} ions in most of the common transition metal compounds during the charge/discharge process.[4] This sluggish diffusion of Mg^{2+} compared to Li^+ is presumed to be due to the strong Mg inter-

actions with the anions and the cations of the hosts, giving rise to a low Mg intercalation level and a large difference between the charge and discharge potentials. The reasons behind the sluggish diffusion of Mg in spinel materials were recently further studied by Ceder *et al.* and Persson *et al.*[25,26] In order to improve this issue, reducing the particle size of the electrode material has been widely used, which significantly shortens the diffusion lengths of ions and electrons within the particles, resulting in more efficient and rapid access of the active cations.[27] Moreover, increased surface area ensures better contact between the electrolyte and active material. This leads to a higher overall ion flux across the electrode-electrolyte interface and accelerated electron migration within the particles.[28]

In an effort to search for potential cathode materials for MIB, manganese-containing compounds have been investigated as attractive materials because of their low cost, environmental friendliness and high natural abundance.[29-31] Among them, MnO_2 is perhaps the most extensively studied electrode material in many kinds of batteries.[32-34] Several polymorphs of MnO_2 have also been investigated as possible MIB cathodes,[35-39] especially α-MnO_2. It showed a high specific capacity of ~280 mAh g^{-1} in the initial discharge, but poor cyclic performance (retained ~50 mAh g^{-1} after just five cycles).[35] Similar rapid attenuation of specific capacity of MnO_2 was also observed by other groups.[35,40] Another manganese oxide, Mn_3O_4, shows a stable spinel structure, in which Mn^{2+} cations are in the tetrahedral sites (8a) and Mn^{3+} cations are in the octahedral sites (16d). Oxides with the spinel structure are another family of materials, which have recently been studied as potential MIB cathodes because of their success in Li-ion batteries. Their favorable properties are attributed to fast ion diffusion resulting from the 3D layered structure, high operating voltage, and structural stability.[41,42] Several studies have claimed intercalation of Mg^{2+} ions into spinel-structured Mn_2O_4 (λ-MnO_2) in aqueous environments.[43,44] Kim *et al.* recently verified that Mg^{2+} ions could be reversibly inserted into spinel structure hosts based on the study of Mn_2O_4.[43] Cao *et al.* showed that Mg^{2+} can intercalate/deintercalate into Mn_2O_4 with a retained capacity of 155 mAh g^{-1} after 300 cycles.[44] However, to date, there is no report on spinel type Mn_3O_4 as cathode material in MIB, which could provide a maximum theoretical capacity of 233 mAh g^{-1} based on one Mg^{2+} intercalation per formula unit (similar to $MgMn_2O_4$[43]). However, according to the equation mentioned by Gregory *et al.*,[45,46] Mn_3O_4 as cathode material for MIB could host about 0.66 Mg ions per formula unit, corresponding to the theoretical capacity of 154 mAh g^{-1}. Thus, in this work, 1C = 154 mA g^{-1}.

The purpose of this work was first to identify an appropriate current collector that have necessary anodic stability in electrolytes for MIB. The materials examined were graphite foil (Gif), Cu foil (Cuf), Ni foil (Nif) and stainless steel foil (SSf). Our results explicitly indicate that Gif is a good candidate as current collector for MIB due to its excellent electrochemical stability over the entire testing potential range in the presence of APC electrolyte. Furthermore, in order to prepare the nanosized Mn_3O_4 particles with high surface area, we provide a facile ultrasonic-assisted method at room temperature without any additional surfactant or template. The as-synthesized Mn_3O_4 nanoparticles with diameters of ~10 nm and high specific surface area of 102 m^2 g^{-1}, exhibit near 100% coulombic efficiencies at different charge rates and good cycling stability (93 % retention after 1000 cycles) as cathode material for MIB. The result is promising as it suggests that the spinel type Mn_3O_4 can be the new candidate for cathode in MIB systems with a Mg metal anode.

2. EXPERIMENTAL SECTION

2.1 Synthesis of Mn_3O_4 nanoparticles

The synthesis of Mn_3O_4 nanoparticles have been reported in previous work.[47] Briefly, 12 mmol $MnCl_2 \cdot 4H_2O$ (2.4 g, Aldrich, 99%) and 100 mL ethanol amine (ETA, Aldrich, 99%) were loaded into a beaker, and then placed in a Branson digital sonifier (Danbury, USA). After ultrasonic processing for 10 min, 200 mL of distilled water was added into the resulting colloid solution. The mixture was subsequently stirred overnight at ambient temperature. The clear brown mixture turned to a dark brown suspension. The suspension was centrifuged at 8000 rpm for 5 min and washed repeatedly with distilled water to remove the residual ETA until the pH of the filtrate was neutral. The Mn_3O_4 nanoparticles were dried at 80 °C in vacuum, and collected as a dark brown powder. The as-synthesized product obtained through the ultrasonic-assisted method was named U-Mn_3O_4 (where U is for ultrasonic). Commercially available Mn_3O_4 (Erachem Comilog), which was named C-Mn_3O_4 (where C is for commercial), was used without further treatment to study the effect of particle size and surface area on the battery performance of Mn_3O_4 as MIB cathode material.

2.2 Preparation of electrolyte

The APC electrolyte solution for MIB was synthesized according to a previously described procedure.[5] Typically, aluminium trichloride ($AlCl_3$, Aldrich, 99.999%) was first mixed with anhydrous tetrahydrofuran (THF, Aldrich) under magnetic stirring to form a transparent solution. Then, phenylmagnesium chloride in THF (PhMgCl in THF, Aldrich, 99%) solution was introduced. The obtained solution was stirred at least 24 hours prior to use. In this work, the molar ratio between PhMgCl and $AlCl_3$ is 2:1, and the concentration was 0.4 mol L^{-1}. All activities were performed in an Ar-filled glove box (<0.1 ppm of water and oxygen), since the electrolyte is moisture sensitive.

2.3 Material Characterization

The powders were analyzed by powder X-ray diffraction (XRD) using Cu Kα radiation (Bruker AXS D8 FOCUS diffractometer with a LynxEye PSD). The samples for ex-situ XRD characterization were prepared inside an Ar-filled glove box. Cycled coin cells were disassembled and the active material was carefully removed from the current collector using a scalpel. The electrodes were washed with THF in order to remove the residual electrolyte and dried overnight at room temperature under vacuum. The nitrogen adsorption-desorption isotherms and pore size distribution were analyzed by nitrogen adsorption measurements (Tristar 3000 Micrometrics). Before the measurements, the sample was degassed at 120 °C under vacuum overnight to eliminate adsorbed water, and the specific surface area was calculated by the Brunauer-Emmett-Teller (BET) method. The morphology of the products was studied using field emission scanning electron microscopy (FESEM, Zeiss Ultra, 55 limited Edition), and transmission electron microscopy (TEM). TEM was performed with a double Cs corrected, coldFEG JEOL ARM200CF, operated at 200 kV. The sample powders were dispersed in ethanol and a droplet was transferred to a holey carbon coated Cu TEM grid. A Kelvin bridge was used for the electrical conductivity measurements.[48] The measurement

range used was 0.01 μΩ to 1000 Ω, and the effective conductivity of the sample powder (σ_E) was calculated from the electrical resistance ($R_{measured}$) using the following equation:

$$\sigma_E = [R_{measured} \frac{S}{H}]^{-1}$$

H is the height of the powder column, *S* is its cross section.

2.4 Electrochemical Measurements

The cathode was prepared by mixing 80 wt% of the as-synthesized sample, 10 wt% of Super-P carbon black and 10 wt% of polyvinylidene difluoride (PVDF, Kynar, reagent grade) in the presence of N-methyl pyrrolidinone (NMP, Aldrich, >99%). The slurry was made by ball milling, followed by tape casting onto different current collectors (Gif, Cuf, Nif and SSf). The electrodes were dried at 120 ºC under vacuum for 10 hours. After that, the dried film was punched into discs with 16 mm diameter. The loading density is about 0.6 mg cm^{-2}. The electrochemical performance of the samples was studied via CR2016 coin cells with a Mg ribbon counter electrode, glass microfiber separator (Whatman), and 0.4 mol L^{-1} APC electrolyte. Before use, the Mg ribbon was polished on both sides with SiC paper, followed by etching in chromic acid for 2 mins, then washed clean with THF and dried overnight under vacuum. Polishing of the Mg ribbon as well as the coin cell assembly was performed inside an Ar-filled glove box. Galvanostatic charge/discharge testing was performed at ambient temperature on an Arbin BT2043 (Texas, USA) battery testing system with the cut-off

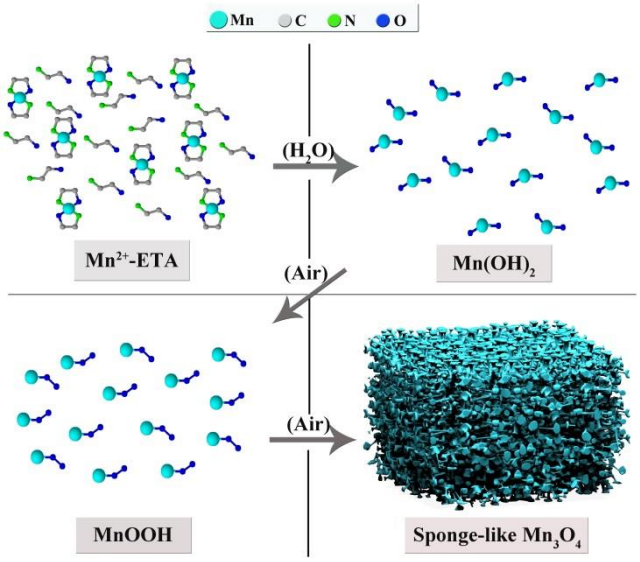

Figure 1. The formation of sponge-like porous Mn_3O_4 nanoparticles.

voltage of 2.1/0.2V vs. Mg. The current rate varied from 0.1C to 10C (1C = 154 mA g^{-1}).

The electrochemical impedance spectra (EIS) and cyclic voltammetry (CV) of the cathodes on different current collectors were assessed, using a 3-electrode cell (EL-CELL) with Mg ribbon as both reference- and counter el ectrode, by a Gamry Reference 600 instrument (Pennsylvania, USA). CV data of the cathodes were collected at potentials between 0.2 and 2.1 V vs. Mg with a scanning rate of 0.2 mV s^{-1}. EIS were measured in the frequency range of 0.01 Hz-10 kHz using 5 mV of AC perturbation, and the collected EIS data were fitted using ZView software.

3. RESULTS AND DISCUSSION

As described in a previous study,[47] the ultrasonic treatment in the synthesis of Mn_3O_4 nanoparticles accelerated the formation of the Mn^{2+}-ETA complex due to the alkaline properties of ETA. The complex was hydrolyzed to $Mn(OH)_2$ when the distilled water was introduced. Due to the instability of $Mn(OH)_2$ in air, it was quickly oxidized to MnOOH, and further oxidized to sponge-like porous Mn_3O_4 nanoparticles, which were well dispersed due to the ultrasonication (Figure 1).

As shown in Figure 2a, all diffraction lines of U-Mn_3O_4 and C-Mn_3O_4 are in good agreement with the tetragonal Mn_3O_4 crystal phase (JCPDS: 04-007-1841). No additional diffraction lines from other phases can be detected, indicating high purity of both the commercial and the as-synthesized Mn_3O_4. The XRD patterns of U-Mn_3O_4 prepared via the ultrasonic-assisted process present much broader diffraction peak shapes compared to the commercial sample C-Mn_3O_4. This can be attributed to the smaller grain size of the Mn_3O_4 synthesized via the ultrasonic-assisted process. The small grain size is also confirmed by FESEM (Figure 3a and 3b) and TEM images (Figure 4a-4c) of U-Mn_3O_4. When the solution is exposed

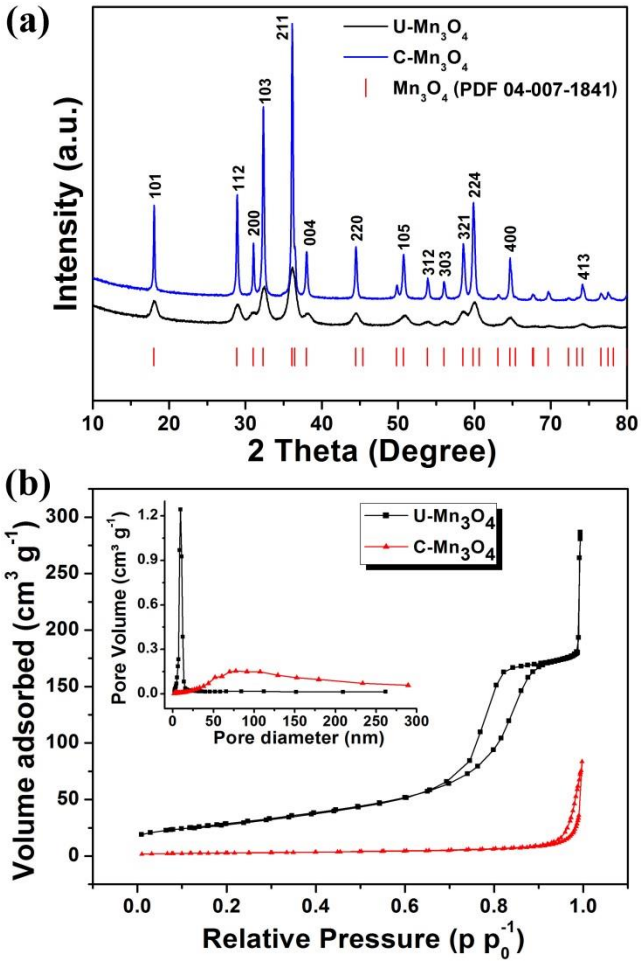

Figure 2. (a) XRD patterns of U-Mn_3O_4, C-Mn_3O_4 and the standard data of Mn_3O_4 from JCPDS card no. 04-007-1841. (b) Nitrogen adsorption/desorption isotherms for U-Mn_3O_4 and C-Mn_3O_4. The inset shows the pore-size distribution for U-Mn_3O_4 and C-Mn_3O_4.

to ultrasonic waves, acoustic cavities form in the liquid, which instantly raise the temperatures to 5000 K and pressures

over 1800 atm in localized area.[49-52] The instant energy of the bubbles generated by ultrasonication results in good dispersibility of the Mn^{2+}-complex precursors. This is beneficial for the following formation of the well-dispersed Mn_3O_4 nanoparticles when the water was introduced. Additionally, the lower crystallinity of U-Mn_3O_4 in contrast with that of C-Mn_3O_4 is due to the ambient temperature synthesis.

The resulting well-dispersed nano-sized particles of U-Mn_3O_4 provided a much higher specific surface area (102 m^2 g^{-1}) than that of C-Mn_3O_4 (9.6 m^2 g^{-1}), which was calculated by the Brunauer-Emmett-Teller (BET) method. The isotherms of U-Mn_3O_4 (Figure 2b) are of IV classification with a clear H1-type hysteresis loop. Combined with the sharp peak centered at around 10 nm in its pore size distribution, this verifies the mesoporous characteristic of the synthesized U-Mn_3O_4. On the other hand, the pore size distribution of C-Mn_3O_4 shows a very weak and broad peak at ~80 nm, and there is no H1 hysteresis loop between the relative pressures of P/P_0 = 0.5 and 0.8, indicating a nearly non-porous structure of C-Mn_3O_4. Moreover, the high content of external surface area (96%, ($S_{mesoporous}$ + $S_{macroporous}$)/S_{total}) of U-Mn_3O_4 allows for easy penetration of the electrolyte in order to utilize all the active surface area and facilitate faster migration of the Mg^{2+} ions. The favoured mass transport of solvated ions from the larger pores to the smaller pores lowers the transport limitation.[53] The nano-scaled host structure shortens the diffusion path for electrons and ions, which results in faster kinetics.[28] This structural configuration of high external surface area with nanosized particles is especially important when the electronic and ionic conductivities of the active material are low. Notably, the MIB performance of Mn_3O_4 strongly depend on the surface area and particle size of the materials, which are discussed in the following sections.

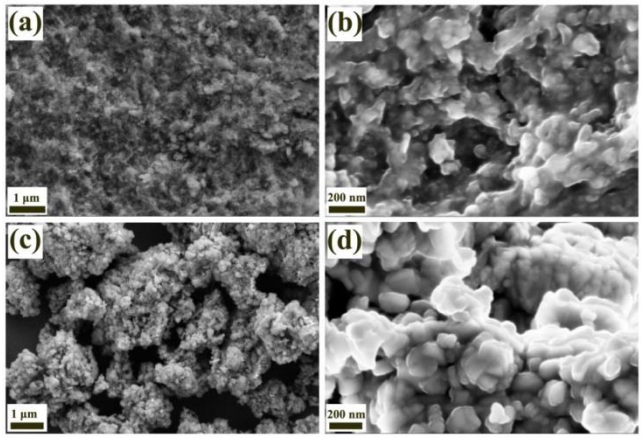

Figure 3. SEM images of (a, b) U-Mn_3O_4 and (c, d) C-Mn_3O_4 with various magnifications.

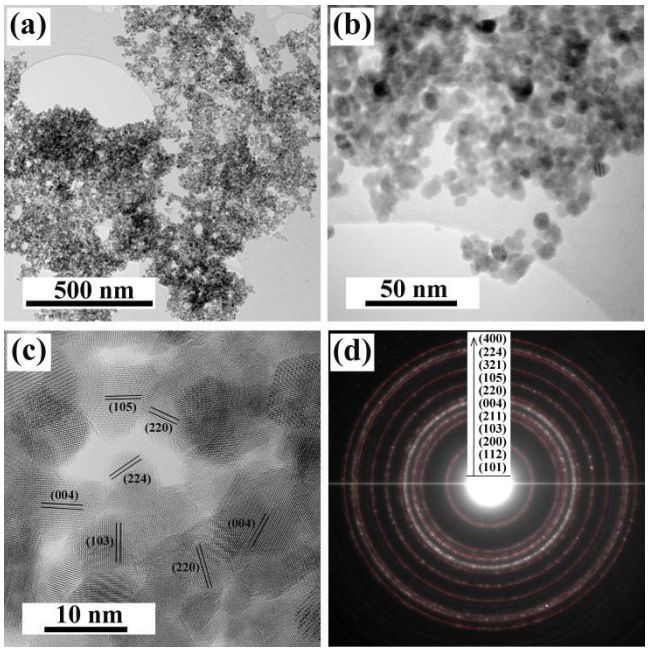

Figure 4. (a-c) TEM micrographs and (d) selected area electron diffraction (SAED) patterns of U-Mn_3O_4 nanoparticles.

The FESEM images of U-Mn_3O_4 obtained via ultrasonication (Figure 3a and 3b) exhibit the sponge-like framework of interconnected pores with well dispersed nanoparticles. This can be more clearly seen in the TEM images. As shown in Figure 4a-4c, U-Mn_3O_4 presents a homogeneous particle size (~10 nm) and good dispersibility. A large amount of mesopores with the size of ~10 nm (which is in accordance with the isotherm and pore size distribution of U-Mn_3O_4 in Figure 2b) can be observed between the aggregated U-Mn_3O_4 nanoparticles. This sponge-like morphology feature is beneficial for the mass transport of solvated Mg ions, as this affords large contact surface area and high utilization of electroactive material, also shown by the BET results. Coupled with a higher electronic conductivity ($4.18 \cdot 10^{-5}$ S m^{-1}), U-Mn_3O_4 exhibits faster kinetics during electrochemical cycling than C-Mn_3O_4 ($6.21 \cdot 10^{-6}$ S m^{-1}), which consists of larger (~150 nm) and severely agglomerated particles (see Figure 3c and 3d). Moreover, Figure 4c and 4d reveal the extremely small and narrow particle size distribution of the synthesized U-Mn_3O_4. All the Mn_3O_4 diffraction rings indexed in the electron diffraction pattern can be identified in the corresponding XRD pattern from the same sample powders (Figure 2a).

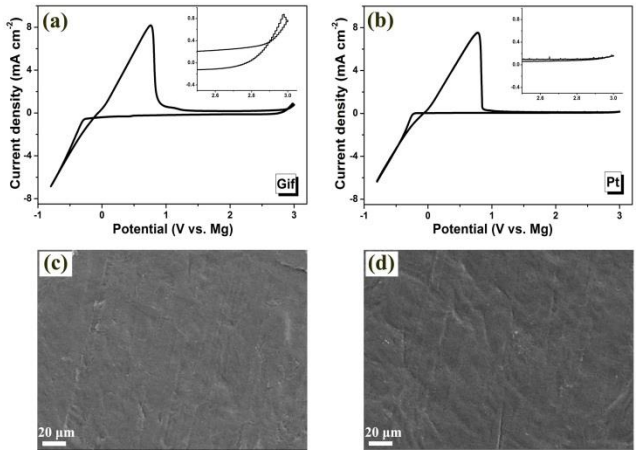

Figure 5. Typical cyclic voltammograms of Mg deposition-stripping in 0.4 M APC electrolyte. Experiments are conducted on a Gif (a) and Pt (b), at a scan rate of 10 mV s^{-1} and room temperature with a Mg metal as reference- and counter electrode. The insets show the enlargements of the area between 2.1 and 3V. SEM images of Gif electrode before (c) and after (d) CV scan between -0.8 V and 3.0 V *vs.* Mg in 0.4 M APC electrolyte.

As reported in previous studies,[22-24] the common metal current collectors such as Nif, Cuf and SSf exhibited limited anodic stability in APC electrolyte. For example, the stable

anodic range of SSf is limited to voltages below 1.2 V, and an obvious anodic peak of Cuf appeared at around 1.7 V, which can also be seen in Figure 6a.[22] In a chloride-rich environment, the severe corrosion behavior on the surface of these metals due to the reactions with chloride anions greatly hinder their development as current collectors for MIB.[9] One obvious concern in this regard is the potential corrosion of the stainless steel casing utilized for the coin cells. In order to exclude any influence on the electrochemical results by corrosion of the casing, CV curves were acquired using the coin cell assembly. In addition, coin cells which were exposed to 1000 cycles were disassembled and inspected. Voltammograms and photographs of the stainless steel casing are presented in the supplementary material, Figure S1 and S2 respectively. The collected data suggests that there is no evident corrosion of the casing, indicating no leakage of the electrolyte from the electrodes or the separator. We can therefore be confident that our results are not affected by any corrosion of the stainless steel coin cell casing.

To characterize the anodic stability of Gif in APC electrolyte, it was first examined by CV using a 3-electrode setup over a potential range of -0.8-3.0 V vs. Mg with 10 mV s^{-1} inside an Argon-filled glove box at room temperature. The cleansed Gif was used as the working electrode. Two pieces of Mg ribbon were used as the counter and reference electrodes after polishing and THF washing. The typical result is shown in Figure 5a. The obvious anodic and cathodic peaks with onsets around 0 V correspond to Mg deposition and dissolution. The shape of Gif´s CV curve is almost identical to that of Pt (see Figure 5b), which is rarely used due to its expensive price. Significant anodic currents due to oxidative decomposition of the APC electrolyte were only observed beyond 2.8 V.[19] The surface morphology of Gif was inspected by SEM before and after dozens of CV cycles, and the obtained images are compared in Figure 5c (before) and Figure 5d (after). Apparently, there is no clear change in surface morphology, which nicely comply with its electrochemical stability in the APC electrolyte. Similar work with Cuf and SSf done by Li *et al*.[3] showed that the initially smooth surface of the metals were damaged during the CV scan, which agree well with other studies.[22,23] In contrast to the metallic materials (Cuf, Nif and SSf), the undoubted advantage of using Gif as current collector in a MIB system is further confirmed in the following discussion.

As shown in Figure 6a and 6b, all measured curves of U-Mn_3O_4 with different metallic current collectors (Nif, Cuf and SSf) exhibit pseudocapacitor-like behavior, i.e. there are no redox peaks in the CV curves (except for a small peak in the Cuf case) and obvious plateaus in the charge/discharge profiles. The corrosion behavior of the metallic materials caused by the APC solution largely increased the contact resistances between the active materials and the current collector, and can even result in some part of the active materials detaching from the current collector. This in turn largely hinders the redox reactions during the electrochemical measurements, which leads to very low specific capacity (~10 mA h g^{-1}) at 0.1C, as shown in Figure 6b. The inclined shape of the CV curve is also an indication of high internal resistance in the electrode. Notably, the cut-off voltages of U-Mn_3O_4-Cuf are 2.0/0.2 V, slightly narrower than that of Nif or SSf (2.1/0.2 V). This was selected based on the high currents in the CV curve of U-Mn_3O_4-Cuf at 2.1 V (Figure 6a). However, there was significant improvement of the specific capacity of U-Mn_3O_4 (~100 mA h g^{-1}, Figure 6c) when Gif was used as current collector. In addition, the specific capacity of pure Gif is only around 0.5 mA h g^{-1} at 20 mA g^{-1} (see Figure S3), which means the improved specific capacity of U-

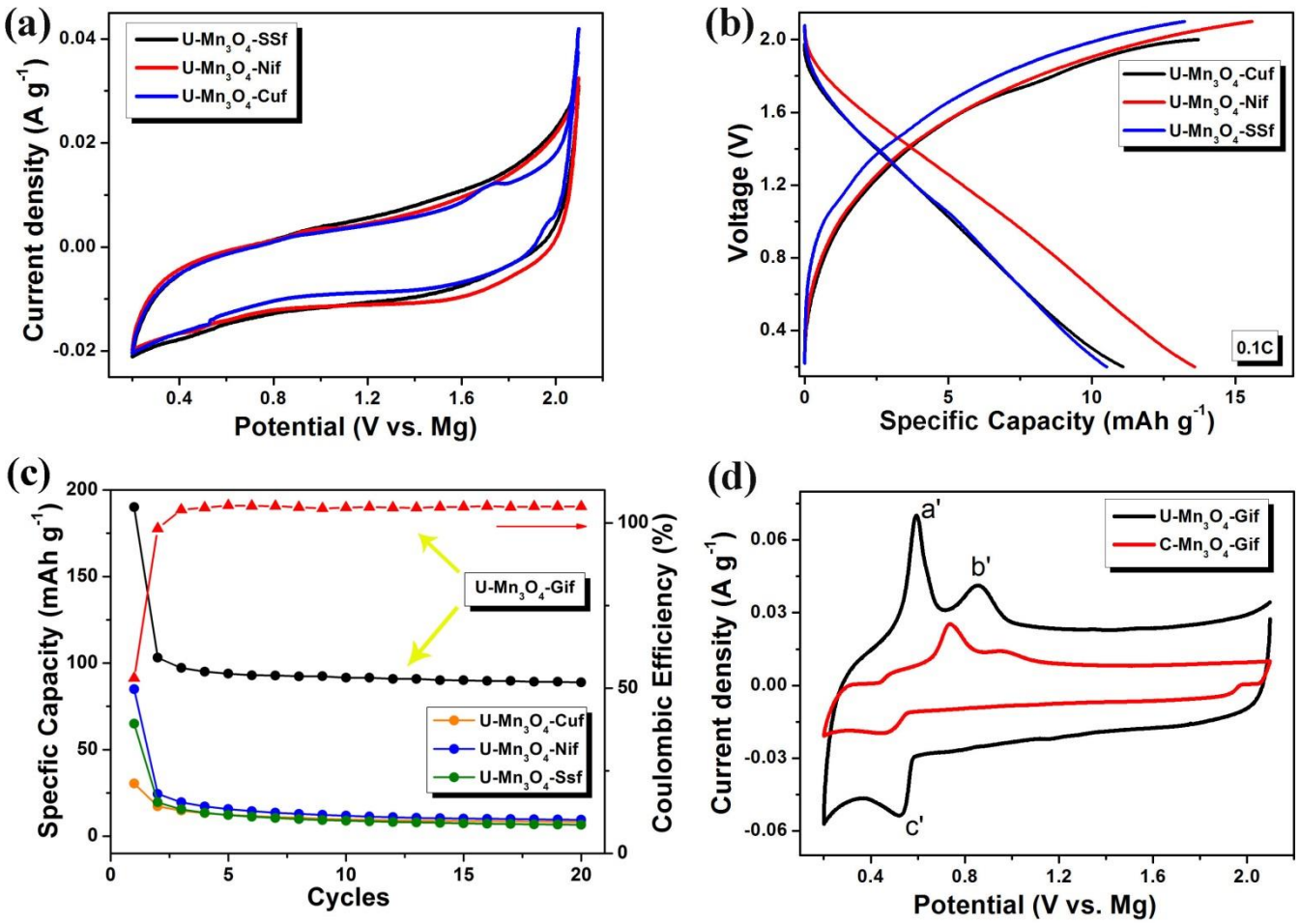

Figure 6. (a) CV curves of U-Mn_3O_4 with different metallic current collectors at the scan rate of 0.2 mV s^{-1}. (b) Galvanostatic charge/discharge profiles of U-Mn_3O_4 (5^{th} cycle) with different metallic current collectors at 0.1C. (c) Cyclic stability of U-Mn_3O_4 with different current collectors at 0.1C. (d) CV curve of U-Mn_3O_4 at the scan rate of 0.2 mV s^{-1} compared with C-Mn_3O_4.

Mn_3O_4-Gif can be attributed to higher electrochemical activity in the active material, and not in the Gif. An excellent cyclic performance and high coulombic efficiency (~105%, the ratio of the charge capacities to the discharge capacities) were also observed (Figure 6c) during the 20 cycles. The slightly larger charge capacities compared to the discharge capacities may be due to some irreversible redox reactions occurring during cycling. The electrochemical stability of the graphite conductive substrate provides good contact with the active material during battery testing, and assures the continued magnesiation/de-magnesiation. The CV scans of U- and C-Mn_3O_4 on Gif, shown in Figure 6d, confirm the electrochemical activity of the two materials. For U-Mn_3O_4-Gif, two anodic peaks a´ (0.59 V), b´ (0.85 V) and one cathodic peak c´ (0.52 V) can be distinguished, attributed to the expected feature of the reversible redox reactions. In contrast to C-Mn_3O_4-Gif, U-Mn_3O_4-Gif shows a higher current response and considerably smaller potential difference between oxidation and reduction, revealing a higher specific capacity and lower polarization during charge/discharge. The reason for this difference is owed to the fast kinetics and high contact surface area of the U-Mn_3O_4 nanoparticles prepared through the ultrasonication-assisted method.

Based on the above discussion, Gif is demonstrated to be a very promising current collector for MIB. The natural chemical inert property of graphite ensures the electrochemical stability of Gif in contact with APC electrolyte, which solution causes severe corrosion of current collectors made from metallic materials. Further studies of U-Mn_3O_4 and C-Mn_3O_4 cathodes with different morphological features were performed based on Gif as the chosen current collector.

The charge/discharge curves of U-Mn_3O_4 and C-Mn_3O_4 cycled between 2.1 and 0.2 V vs. Mg at 0.1 C are shown in Figure 7a and 7b, respectively. U-Mn_3O_4 shows significant capacity loss between the first discharge (190 mAh g^{-1}) and second charge (103 mAh g^{-1}). C-Mn_3O_4 also shows similar behavior in Figure 7b. The initial capacity loss may be caused in part by the electrolyte decomposition and the irreversible redox reactions occurring at the electrode-electrolyte interphase which is caused by the multiple complexes in the APC electrolyte.[19] More probably, the irreversible conversion between Mg and MgO might be an important factor. However, this not confirmed. Lately, Ling *et al.* proved that the discharge product was composed of a core-shell like morphology when they applied MnO_2 as cathode material for MIB. The shell was identi-

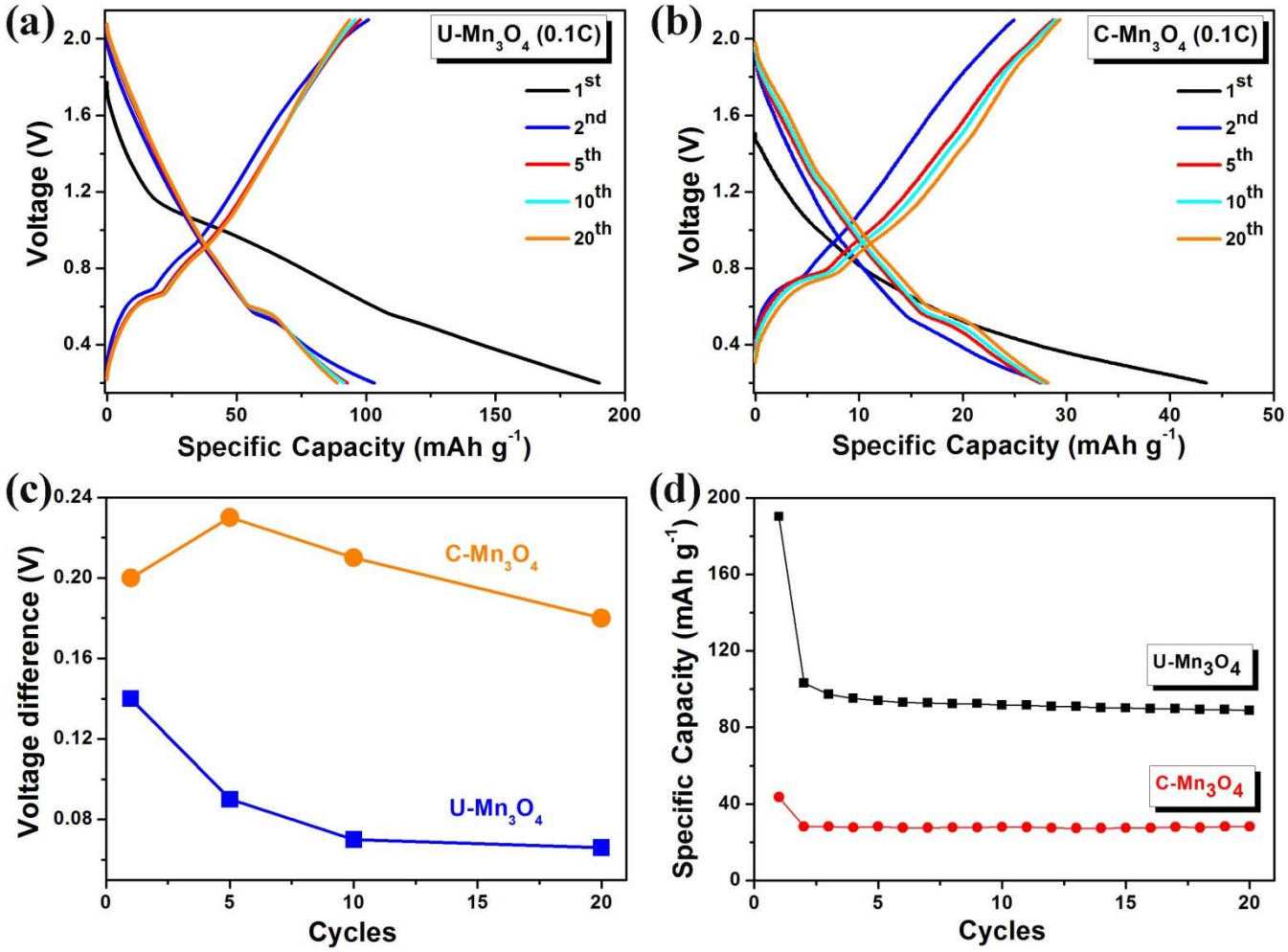

Figure 7. (a,b) Galvanostatic charge/discharge profiles of U-Mn_3O_4 and C-Mn_3O_4 at 0.1C. (c) The voltage difference between charge and discharge plateau at 0.1C. (d) Cyclic stability of U-Mn_3O_4 and C-Mn_3O_4 at 0.1C.

fied as amorphous magnesium oxide mixed with reduced manganese oxide, while the core remains crystalline.[54,55] The thermodynamic driving force for this conversion reaction is attributed to the high stability of MgO.

Except for the first cycle (the initial discharge), a charge capacity of 103 mAh g^{-1} and discharge capacity of 102 mAh g^{-1} in the second cycle (see Figure 7a) result in a coulombic efficiency close to 100%, which remained nearly unchanged in the following cycles. Furthermore, two voltage plateaus are observed during charging, one obvious at about 0.64 V and another barely visible at about 0.90 V. During discharge only one plateau can be observed, at about 0.57 V. In contrast to the CV peaks in Figure 6d, a slight shift of ~0.05 V between the charge/discharge plateaus and anodic/cathodic peaks can be observed. This might be due to the different measuring mechanisms between galvanostatic charge/discharge and cyclic voltammetry, and also due to the different cell systems used (two electrode coin cell for charge/discharge measurement and three electrode EL-cell for CV scanning). After the second cycle, the discharge plateau increases slightly, while the charge plateau shows a slight decrease, thus the voltage difference between charge and discharge (V_{ch} - V_{dis}) becomes smaller with cycling (see Figure 7c). This illustrates improved kinetics of U-Mn_3O_4. The lower this difference, the closer the electrode is to the equilibrium potential, and the lower the kinetic limitations. It is especially noted that the U-Mn_3O_4 nanoparticles have smaller electrochemical polarization than C-Mn_3O_4, which perfectly match the above CV results in Figure 6d. The short term cycling shown in Figure 7d further verify the prominent improvement in the electrochemical response of the systems by the use of sponge-like Mn_3O_4 nanoparticles as the cathode for MIB. U-Mn_3O_4 exhibits much higher specific capacity than C-Mn_3O_4. The reversible specific capacity of U-Mn_3O_4 remains at a value of ~100 mAh g^{-1} for all of the cycles, demonstrating good cycling stability. The particle size and surface area are critical for obtaining high reversible capacity for transition metal oxides with low electrical conductivity. Herein, the sponge-like porous morphology with well dispersed and uniform nanoparticles obtained via the ultrasonication-assisted method is absolutely vital in order for Mn_3O_4 to achieve good battery performance. As shown in Figure 8a, the electrolyte can penetrate into every part of the U-Mn_3O_4 through the interconnected mesopores, which ensures the fast approaching of Mg cations from the electrolyte to the active sites in the host

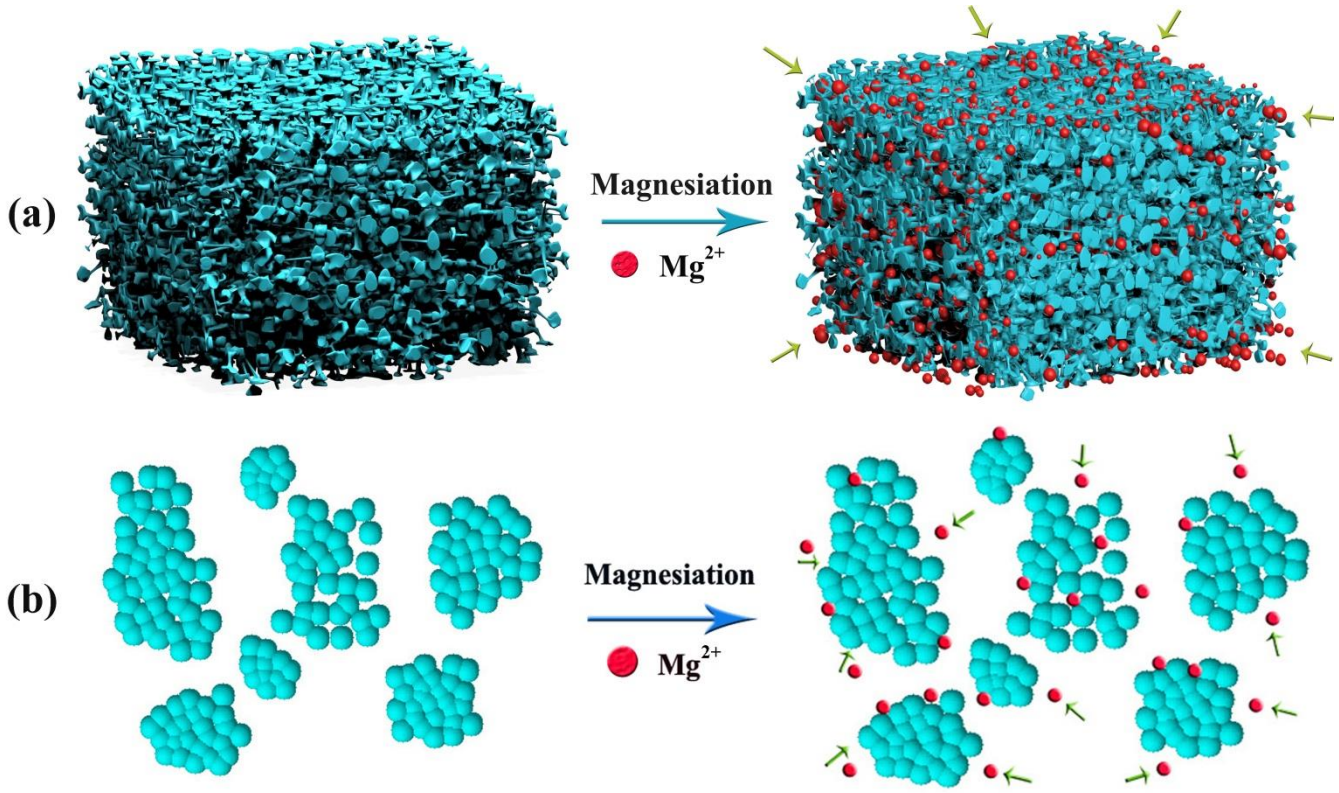

Figure 8. Comparsion of the magnesiation process between (a) U-Mn_3O_4 and (b) C-Mn_3O_4 cathodes for MIB.

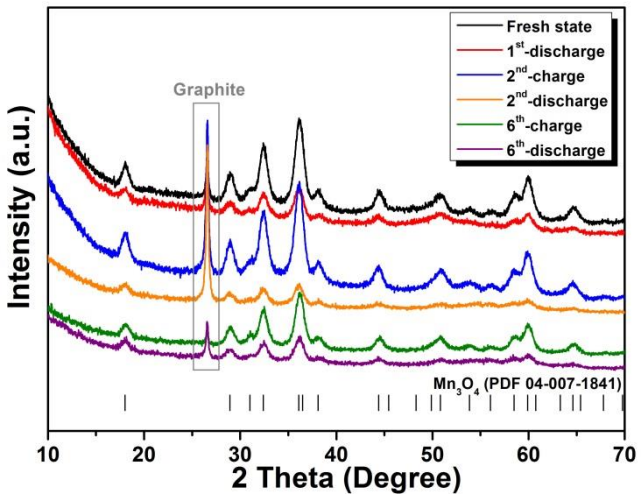

Figure 9. Ex-situ XRD patterns of the U-Mn_3O_4 electrodes at different cell states under 0.1C. The graphite peak is caused by the residual from Gif.

structure, providing high utilization of the active material. For the agglomerated C-Mn_3O_4 particles, the low utilization during magnesiation is illustrated in Figure 8b, only the outer surface of the particles were utilized. This results in poor battery performance of the C-Mn_3O_4 (see Figure 7).

Up to now, several studies have claimed intercalation of Mg^{2+} into spinel-structured Mn_2O_4 (λ-MnO_2) in aqueousenvironments,[43,56] but the mechanism of the Mg insertion reaction into spinel-type Mn_3O_4 have not been ascertained. The results of Cabana *et al.*[43] provided direct visu-

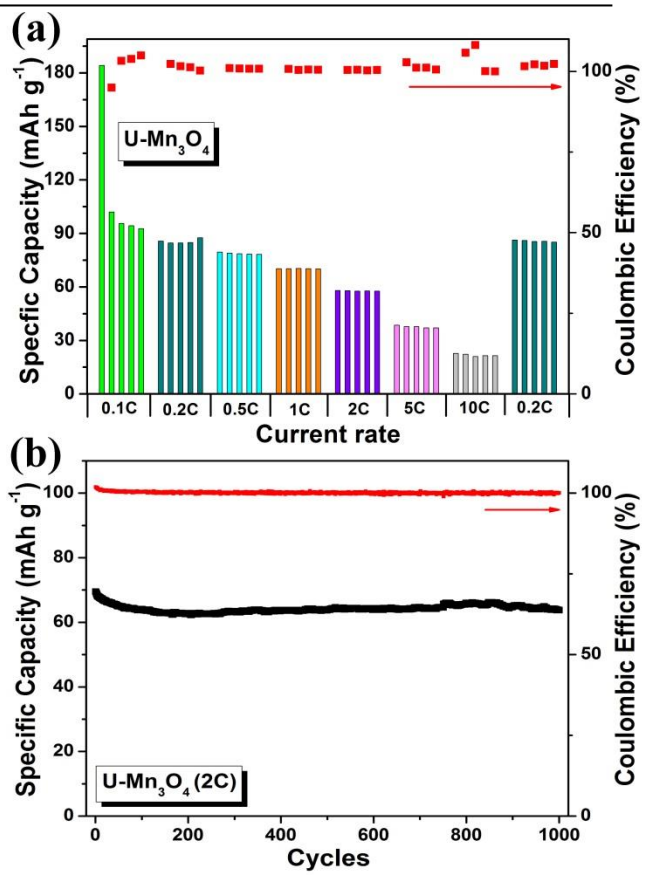

Figure 10. (a) Rate cyclic performance of U-Mn_3O_4. (b) Long cycle life of U-Mn_3O_4 at 2C.

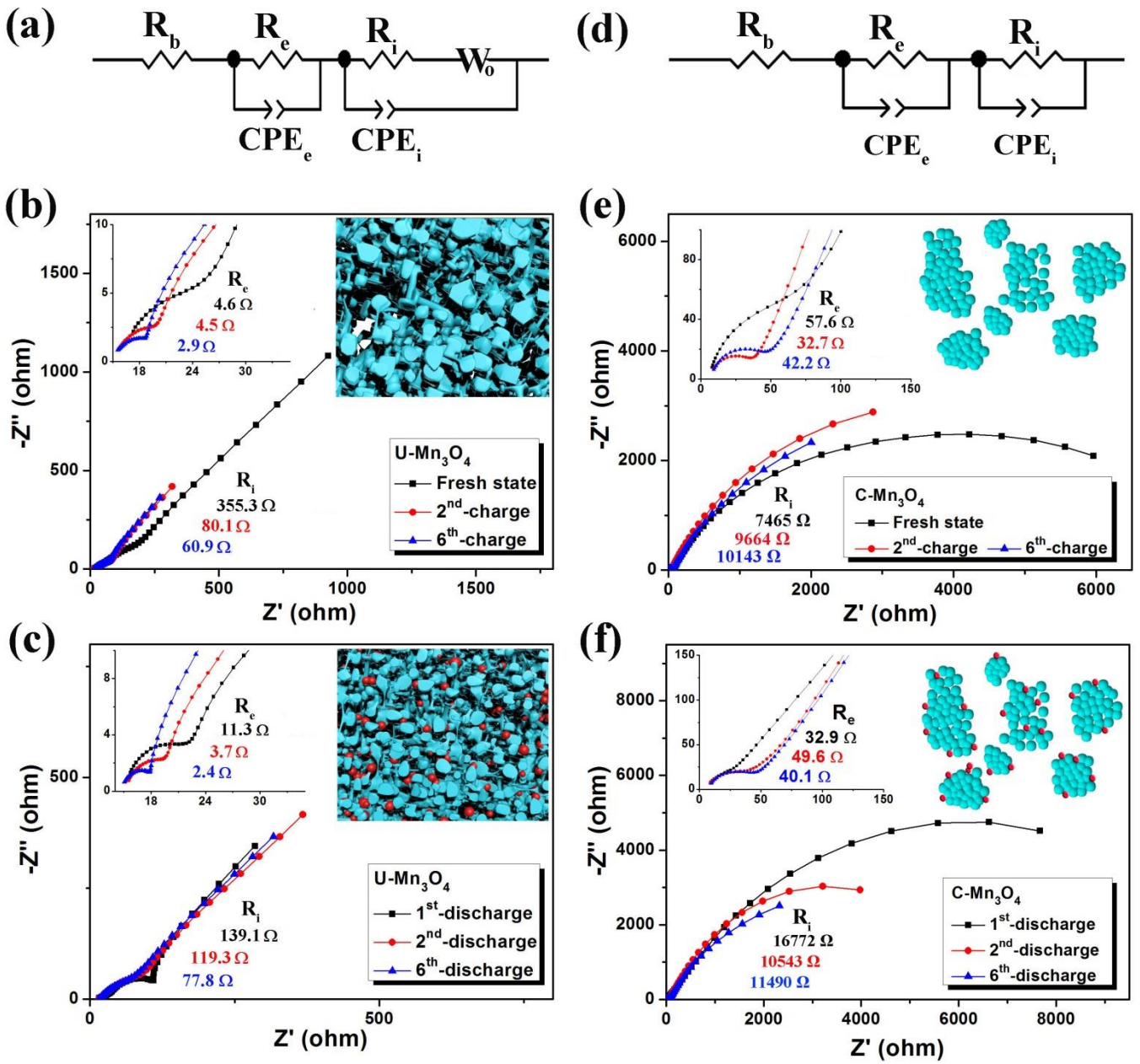

Figure 11. The equivalent circuits of (a) U-Mn_3O_4 and (d) C-Mn_3O_4. The Nyquist plots of (b, c) U-Mn_3O_4 and (e, f) C-Mn_3O_4 electrodes at different cell states under the current density of 0.1 C in the frequency range of 10^4 Hz to 0.01 Hz. The left insets in Figure 11b, 11c, 11e and 11f show the high-frequency region of the Nyquist plot of U/C-Mn_3O_4, and the right insets illustrate the states of samples after discharge or charge measurements.

alization of Mg^{2+} inserting into the tetrahedral sites of the spinel-host Mn_2O_4 in an aqueous electrolyte. The rever-sibility of this intercalation was verified. Interestingly, Ichitsubo *et al.*[56] demonstrated that the Mg insertion into spinel lattices occurs via an "intercalation and push-out" process. The Mg^{2+} cation is inserted into an octahedral site-16c, and the original cation located in the neighboring tetrahedral site-8a migrates to an adjacent 16c site due to the repulsion between the cations. Although the results presented are contradictory, they can still be a good guidance for further research on spinel-type Mn_3O_4. In this work, ex-situ XRD characterization of U-Mn_3O_4 electrodes cycled at 0.1C was performed in order to investigate charge/discharge mechanisms. The XRD pattern of the pristine electrode in Figure 9 shows a set of broad diffraction peaks corresponding to the tetragonal Mn_3O_4 crystal phase (JCPDS 04-007-1841). What can quite clearly be observed is that the intensity of the peaks changes during cycling. Upon the first discharge the peak intensities were reduced dramatically. When the battery was charged again (2^{nd} charge), the intensity of the peaks recovered. This same trend was also observed on the following cycles, and you see a periodic change in XRD peak intensities. On the other hand, no clear peak shifts or new Bragg reflections were observed, indicating that no new phases were formed during charge/discharge. This observation excludes the possibility of intercalation in the Mn_3O_4-APC system, at least to any significant extent. Th-

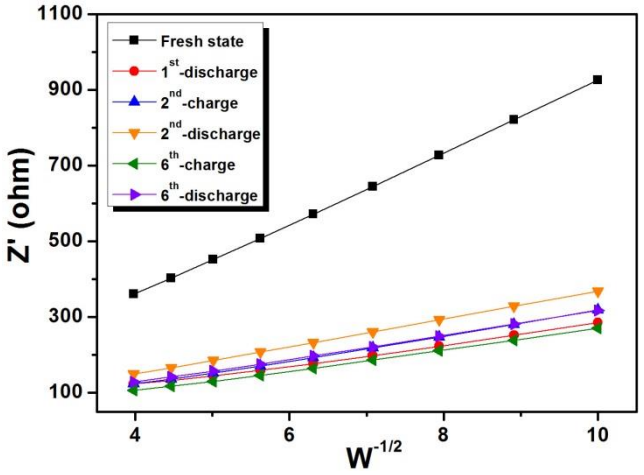

Figure 12. The plots of the real part of impedance as a function of the inverse square root of angular frequency at different stages in the Warburg region for U-Mn_3O_4.

ere is a possibility that Mg could go into the outer surface layer of the particles. However, this would most likely be below the detection limit for conventional XRD. Moreover, the CV curve of U-Mn_3O_4 shows the same shape with that of Gif (see Figure S4). This means that Mn_3O_4 was not involved in the reactions occurring during the charge and discharge process. The charge/discharge mechanism of the Mn_3O_4 cathode shows more resemblance to a pseudocapacitor. Here, the total stored charge can be divided into two parts: pseudocapacitance (contributed from surface redox reactions) and double layer capacitance which contributes about ~ 90% (which can be confirmed from the CV curve in Figure 6d). Spongy-like Mn_3O_4 nanoparticles with large surface area provide numerous active sites for storing Mg cations, and produce a large double layer capacitance. The active species are identified to be RMg^+ ($MgCl^+$ or $Mg_2Cl_3^+$) coordinated by THF, according to the research of Canepa *et. al.*[16] Recently, Aurbach *et al.* revealed that the activity and composition of the MACC electrolyte (the magnesium aluminum chloride complex electrolyte, similar composition with APC electrolyte) varies with cycling.[57] Furthermore, the work done by Gewirth *et al.* showed that the coordinated THF molecules (which with RMg^+ species formed at the surface of electrode) are more easily oxidized to GBL (γ-butyrolactone) due to the presence of Lewis acidity of RMg^+, compared with the uncoordinated THF molecules.[14,58] This reaction is irreversible and THF molecules are continuously consumed during cycling. However, it does not affect the cycling stability due to the large content of THF molecules present in the APC electrolyte. There are probably other side reactions going on as well. However, they are not yet understood. The redox peaks appearing in the CV curves may be due to these side reactions which produce a small amount of pseudocapacitance. Therefore, similar with the case in a pseudocapacitor, preparation of nano-structured materials with large surface area can be a very efficient method to enhance the electrochemical performance.

Rate performances for U-Mn_3O_4 nanoparticles at various current densities from 0.1C to 10C are shown in Figure 10a. The specific capacity of U-Mn_3O_4 gradually decreases with the increasing current densities, but after the initial irreversible capacity loss at 0.1C, the capacity remains quite stable and the coulombic efficiency is near 100% at each current rate. After galvanostatic charge/discharge cycles at current densities from 0.1C to 10C, the capacity fully returns back to the initial value when the battery is cycled at 0.2C again. Long cycling performance is a key factor in determining the suitability of the battery electrodes for practical applications. As shown in Figure 10b, the cycling tests for 1000 cycles were carried out at 2C. 94% of the initial capacity of U-Mn_3O_4 was retained after 1000 cycles. Moreover, the high coulombic efficiency at 2C unambiguously demonstrates that the Mn_3O_4-APC system is quite stable and the spinel-type Mn_3O_4 is a very promising cathode candidate for MIB, especially with nano-sized particles and high surface area.

In order to understand why U-Mn_3O_4 exhibits much better electrochemical performance than C-Mn_3O_4, EIS studies were performed on the freshly prepared Mn_3O_4 electrode as well as cycled Mn_3O_4 electrode at different stages. The suggested equivalent circuits are given in Figures 11a and 11d. Although the detailed charge/discharge mechanism for the Mn_3O_4 cathode has not been ascertained yet, the frequency dispersion and impedance shape indicates that R_b is the total resistance contribution from the electrolyte, separator, and electrodes; R_e and CPE_e are the resistance and capacitance due to the electron transfer through the Mn_3O_4 electrode/APC electrolyte interface, which correspond to the first semicircle at high frequencies (HFS); R_i and CPE_i in the low frequency semi-circle (LFS) region can be attributed to Mg-ion trapping in the cathode host (R_i);[59] a straight line in the low-frequency range (Warburg behavior) is typically associated with the solid state diffusion of Mg^{2+} ions in the bulk Mn_3O_4.

Markedly, from the Nyquist plots of U-Mn_3O_4 in Figures 11b and 11c, a clear decrease of R_e can be observed during both the de-magnesiation process (2nd charge and 6th charge in Figure 11b) and the magnesiation process (1st discharge, 2nd discharge and 6th discharge in Figure 11c). The value of R_e, around 5 Ω, is much lower than those of the general MIB,[60-63] which is a benefit from the sponge-like morphology features of the U-Mn_3O_4 nanoparticles. The same tendency in R_e also appeared in LFS of the Nyquist plots of U-Mn_3O_4. The decrease in both R_e and R_i signifies the low polarization of U-Mn_3O_4 during cycling, which is consistent with the result from the galvanostatic charge/discharge measurements. Meanwhile, for all cycles there is a 45° slope in the Warburg range, typically attributed to diffusion limitations. The Warburg coefficient (σ_W) at different stages can be obtained from the slope of Z' vs. $\omega^{-1/2}$ plots (ω is the angular frequency) in the Warburg region (Figure 12). σ_W remained almost unchanged during the charge/discharge process. This means the stable host structure of the synthesized U-Mn_3O_4 provides a near constant diffusion rate of Mg ions in the bulk Mn_3O_4, which ensures the good cyclic stability shown in Figure 10b. On the other hand, the C-Mn_3O_4 agglomerates show larger and irregular values for R_e, and a very large LFS (two orders of magnitude larger than that of U-Mn_3O_4) without the linear Warburg response (see Figure 11e and 11f). These results can also explain the poor electrochemical performance of C-Mn_3O_4 in Figure 7.

4 CONCLUSIONS

It has been demonstrated that Gif is a better choice as current collector for MIB due to its higher electrochemical stability compared to the typical metals, which have severe corrosion problems in APC electrolyte. Using Gif as the current collector, a spinel-type Mn_3O_4 has been investigated as cathode material for MIB, and the effect of particle size and surface

area of Mn_3O_4 on electrochemical performance have been studied. The synthesized sponge-like U-Mn_3O_4 with high content of interconnected mesopores and well-dispersed nanoparticles (~10 nm) presents a remarkable enhancement in the performance as cathode for MIB, i.e. high coulombic efficiency and good cyclic stability. The result is promising as it suggests that a spinel-Mn_3O_4 cathode can be the new candidate for MIB. We strongly believe that this study will open the way for exploring more spinel-structured compounds for MIB.

■ ASSOCIATED CONTENT

Supporting Information

Cyclic voltammograms of Mg deposition-stripping in 0.4 M APC electrolyte with coin cell as working electrode. The photographs of a dissembled coin cell after 1000 cycles charge/discharge. Cyclic stability of pure Gif cycled at 20 mA g^{-1}. CV curve of U-Mn_3O_4 at the scan rate of 0.2 mV s^{-1} compared with pure Gif.

■ AUTHOR INFORMATION

Corresponding Author

*E-mail: fride.vullum-bruer@ntnu.no

Notes

The authors declare no competing financial interest.

■ ACKNOWLEDGMENTS

This work was sponsored by the Research Council of Norway through the project NanoMag (Grant no. 221785). Erachem Comilog is acknowledged for providing the commercial Mn_3O_4 powders free of charge.

■ REFERENCES

(1) Aurbach, D.; Lu, Z.; Schechter, A.; Gofer, Y.; Gizbar, H.; Turgeman, R.; Cohen, Y.; Moshkovich, M.; Levi, E. Prototype Systems for Rechargeable Magnesium Batteries. *Nature* **2000**, *407*, 724 - 727.

(2) Wu, N.; Yang, Z. Z.; Yao, H. R.; Yin, Y. X.; Gu, L.; Guo, Y. G. Improving the Electrochemical Performance of the $Li_4Ti_5O_{12}$ Electrode in a Rechargeable Magnesium Battery by Lithium-Magnesium Co-Intercalation. *Angew. Chem. Int. Ed.* **2015**, *54*, 1-6.

(3) Cheng, Y. W.; Liu, T. B.; Shao, Y. Y.; Engelhard, M. H.; Liu, J.; Li, G. S. Electrochemically Stable Cathode Current Collectors for Rechargeable Magnesium Batteries. *J. Mater. Chem. A* **2014**, *2*, 2473-2477.

(4) Levi, E.; Gofer, Y.; Aurbach, D. On the Way to Rechargeable Mg Batteries: The Challenge of New Cathode Materials. *Chem. Mater.* **2010**, *22*, 860-868.

(5) Yoo, H. D., Shterenberg, I.; Gofer, Y.; Gershinsky, G.; Pour, N.; Aurbach, D. Mg Rechargeable Batteries: an On-going Challenge. *Energy Environ. Sci.* **2013**, *6*, 2265-2279.

(6) Liang, Y. L.; Yoo, H. D.; Li, Y. F.; Shuai, J.; Calderon, H. A.; Hernandez, F. C. R.; Grabow, L. C.; Yao, Y. Interlayer-Expanded Molybdenum Disulfide Nanocomposites for Electrochemical Magnesium Storage. *Nano Lett.* **2015**, *15*, 2194-2202.

(7) Ling, C.; Banerjee, D.; Matsui, M. Study of the Electrochemical Deposition of Mg in the Atomic Level: Why it Prefers the Non-dendritic Morphology. *Electrochim. Acta* **2012**, *76*, 270-274.

(8) Aurbach, D.; Suresh, G. S.; Levi, E.; Mitelman, A.; Mizrahi, O.; Chusid, O.; Brunelli, M. Progress in Rechargeable Magnesium Battery Technology. *Adv. Mater.* **2007**, *19*, 4260-4267.

(9) Muldoon, J.; Bucur, C. B.; Oliver, A. G.; Sugimoto, T.; Matsui, M.; Kim, H. S.; Allred, G. D.; Zajicek, J.; Kotani, Y. Electrolyte Roadblocks to a Magnesium Rechargeable Battery. *Energy Environ. Sci.* **2012**, *5*, 5941-5950.

(10) Tutusaus, O.; Mohtadi, R.; Arthur, T. S.; Mizuno, F.; Nelson, E. G.; Sevryugina, Y. V. An Efficient Halogen-Free Electrolyte for Use in Rechargeable Magnesium Batteries. *Angew. Chem. Int. Ed.* **2015**, *54*, 7900-7904.

(11) Canepa, P.; Jayaraman, S.; Cheng, L.; Rajput, N. N.; Richards, W. D.; Gautam, G. S.; Curtiss, L. A.; Perssond, K. A.; Ceder, G. Elucidating the Structure of the Magnesium Aluminum Chloride Complex Electrolyte for Magnesium-Ion Batteries. *Energy Environ. Sci.* **2015**, *8*, 3718-3730.

(12) Doe, R. E.; Han, R.; Hwang, J.; Gmitter, A. J.; Shterenberg, I.; Yoo, H. D.; Pour, N.; Aurbach, D. Novel, Electrolyte Solutions Comprising Fully Inorganic Salts with High Anodic Stability for Rechargeable Magnesium Batteries. *Chem. Commun.* **2014**, *50*, 243-245.

(13) Kim, H. S.; Arthur, T. S.; Allred, G. D.; Zajicek, J.; Newman, J. G.; Rodnyansky, A. E.; Oliver, A. G.; Boggess, W. C.; Muldoon, J. Structure and Compatibility of a Magnesium Electrolyte with a Sulphur Cathode. *Nat. Commun.* **2011**, *2*, 427-432.

(14) Barile, C. J.; Spatney, R.; Zavadil, K. R.; Gewirth, A. A. Investigating the Reversibility of in Situ Generated Magnesium Organohaloaluminates for Magnesium Deposition and Dissolution. *J. Phys. Chem. C* **2014**, *118*, 10694-10699.

(15) Barile, C. J.; Barile, E. C.; Zavadil, K. R.; Nuzzo, R. G.; Gewirth, A. A. Electrolytic Conditioning of a Magnesium Aluminum Chloride Complex for Reversible Magnesium Deposition. *J. Phys. Chem. C* **2014**, *118*, 27623-27630.

(16) Canepa, P.; Gautam, G. S.; Malik, R.; Jayaraman, S.; Rong, Z.; Zavadil, K. R.; Persson, K.; Ceder, G. Understanding the Initial Stages of Reversible Mg Deposition and Stripping in Inorganic Nonaqueous Electrolytes. *Chem. Mater.* **2015**, *27*, 3317-3325.

(17) Shao, Y.; Liu, T.; Li, G.; Gu, M.; Nie, Z.; Engelhard, M.; Xiao, J.; Lv, D.; Wang, C.; Zhang, J. G.; Liu, J. Coordination Chemistry in Magnesium Battery Electrolytes: How Ligands Affect Their Performance. *Sci. Rep.* **2013**, *3*, 3130-3136.

(18) Aurbach, D.; Gizbar,; Schechter, H. A.; Chusid, O.; Gottlieb, H. E.; Gofer, Y.; Goldberg, I. Electrolyte Solutions for Rechargeable Magnesium Batteries Based on Organomagnesium Chloroaluminate Complexes. *J. Electrochem. Soc.* **2002**, *149*, A115-A121.

(19) Pour, N.; Gofer, Y.; Major, D. T.; Aurbach, D. Structural Analysis of Electrolyte Solutions for Rechargeable Mg Batteries by Stereoscopic Means and DFT Calculations. *J. Am. Chem. Soc.* **2011**, *133*, 6270-6278.

(20) Carter, T. J.; Mohtadi, R.; Arthur, T. S.; Mizuno, F.; Zhang, R.; Shirai, S.; Kampf, J. W. Boron Clusters as Highly Stable Magnesium-Battery Electrolytes. *Angew. Chem., Int. Ed.* **2014**, *53*, 3173-3177.

(21) Piccolo, M.; Giffin, G. A.; Vezzu, K.; Bertasi, F.; Alotto, P.; Guarnieri, M.; Noto, V. D. Molecular Relaxations in Magnesium Polymer Electrolytes via GHz Broadband Electrical Spectroscopy. *ChemSusChem* **2013**, *6*, 2157-2160.

(22) Lv, D. P.; Xu, T.; Saha, P.; Datta, M. K.; Gordin, M. L.; Manivannan, A.; Kumta, P. N.; Wang, D. H. A Scientific Study of Current Collectors for Mg Batteries in $Mg(AlCl_2EtBu)_2$/THF Electrolyte. *J. Electrochem. Soc.* **2013**, *160*, A351-A355.

(23) Yagi, S.; Tanaka, A.; Ichikawa, Y.; Ichitsubo, T.; Matsubara, E. Electrochemical Stability of Magnesium Battery Current Collectors in a Grignard Reagent-Based Electrolyte. *J. Electrochem. Soc.* **2013**, *160*, C83-C88.

(24) Yagi, S.; Tanaka, A.; Ichitsubo, T.; Matsubara, E. Electrochemical Stability of Metal Electrodes for Reversible Magnesium Deposition/Dissolution in Tetrahydrofuran Dissolving Ethylmagnesium Chloride. *ECS Electrochem. Lett.* **2012**, *1*, D11-D14.

(25) Liu, M.; Rong, Z.; Malik, R.; Canepa, P.; Jain, A.; Cederb, G.; Persson, K. A. Spinel Compounds as Multivalent Battery Cathodes: a Systematic Evaluation Based on *AB Initio* Calculations. *Energy Environ. Sci.* **2015**, *8*, 964-974.

(26) Rong, Z.; Malik, R.; Canepa, P.; Gautam, G. S.; Liu, M.; Jain, A.; Persson, K.; Ceder, G. Materials Design Rules for Multivalent Ion

Mobility in Intercalation Structures. *Chem. Mater.* **2015**, *27*, 6016-6021.

(27) Saha, P.; Datta, M. K.; Velikokhatnyi, O. I.; Manivannan, A.; Alman, D.; Kumta, P. N. Rechargeable Magnesium Battery: Current Status and Key Challenges for the Future. *Prog. Mater. Sci.* **2014**, *66*, 1-86.

(28) Zheng, Y. P.; NuLi, Y. N.; Chen, Q.; Wang, Y.; Yang, J.; Wang, J. L. Magnesium Cobalt Silicate Materials for Reversible Magnesium Ion Storage. *Electrochim. Acta* **2012**, *66*, 75-81.

(29) Wang, L.; Chen, L.; Li, Y. H.; Ji, H. M.; Yang, G. Preparation of Mn_3O_4 Nanoparticles at Room Condition for Supercapacitor Application. *Powder Technol.* **2013**, *235*, 76-81.

(30) Tan, Y. W.; Meng, L.; Peng, Q.; Li, Y. D. One-Dimensional Single-Crystalline Mn_3O_4 Nanostructures with Tunable Length and Magnetic Properties of Mn_3O_4 Nanowires. *Chem. Commun.* **2011**, *47*, 1172-1174.

(31) Hu, C. C.; Wu, Y. T.; Chang, K. H. Low-Temperature Hydrothermal Synthesis of Mn_3O_4 and MnOOH Single Crystals: Determinant Influence of Oxidants. *Chem. Mater.* **2008**, *20*, 2890-2894.

(32) Ling, C.; Mizuno, F. Capture Lithium in αMnO_2: Insights from First Principles. *Chem. Mater.* **2012**, *24*, 3943-3951.

(33) Débart, A.; Paterson, A. J.; Bao, J.; Bruce, P. G. α-MnO2 Nanowires: A Catalyst for the O_2 Electrode in Rechargeable Lithium Batteries. *Angew. Chem. Int. Ed.* **2008**, *47*, 4521-4524.

(34) Johnson, C. S. Development and Utility of Manganese Oxides as Cathodes in Lithium Batteries. *J. Power Sources* **2007**, *165*, 559-565.

(35) Zhang, R.; Yu, X.; Nam, K. W.; Ling, C.; Arthur, T. S.; Song, W.; Knapp, A.; Ehrlich, S. N.; Yang, X. Q.; Matsui, M. α-MnO_2 as a Cathode Material for Rechargeable Mg Batteries. *Electrochem. Commun.* **2012**, *23*, 110-113.

(36) Rasul, S.; Suzuki, S.; Yamaguchi, S.; Miyayama, M. Manganese Oxide Octahedral Molecular Sieves as Insertion Electrodes for Rechargeable Mg Batteries. *Electrochim. Acta* **2013**, *110*, 247-252.

(37) Ling, C.; Mizuno, F. Phase Stability of Post-spinel Compound AMn_2O_4 (A = Li, Na, or Mg) and Its Application as a Rechargeable Battery Cathode. *Chem. Mater.* **2013**, *25*, 3062-3071.

(38) Nam, K. W.; Kim, S.; Lee, S.; Salama, M.; Shterenberg, I.; Gofer, Y.; Kim, J. S.; Yang, E.; Park, C. S.; Kim, J. S.; Lee, S. S.; Chang, W. S.; Doo, S. G.; Jo, Y. N.; Jung, Y.; Aurbach, D.; Choi, J. W. The High Performance of Crystal Water Containing Manganese Birnessite Cathodes for Magnesium Batteries. *Nano Lett.* **2015**, *15*, 4071-4079.

(39) Sun, X.; Duffort, V.; Mehdi, B. L.; Browning, N. D.; Nazar, L. F. Investigation of the Mechanism of Mg Insertion in Birnessite in Nonaqueous and Aqueous Rechargeable Mg-Ion Batteries. *Chem. Mater.* **2016**, *28*, 534-542.

(40) Rasul, S.; Suzuki, S.; Yamaguchi, S.; Miyayama, M. High Capacity Positive Electrodes for Secondary Mg-Ion Batteries. *Electrochim. Acta* **2012**, *82*, 243-249.

(41) Manthiram, A. Materials Challenges and Opportunities of Lithium Ion Batteries. *J. Phys. Chem. Lett.* **2011**, *2*, 176-184.

(42) Knight, J. C.; Therese, S.; Manthiram, A. On the Utility of Spinel Oxide Hosts for Magnesium-Ion Batteries. *ACS Appl. Mater. Interfaces* **2015**, *7*, 22953-22961.

(43) Kim, C.; Phillips, J.; Key, P. B.; Yi, T.; Nordlund, D.; Yu, Y. S.; Bayliss, R. D.; Han, S. D.; He, M.; Zhang, Z.; Burrell, A. K.; Klie, R. F.; Cabana, J. Direct Observation of Reversible Magnesium Ion Intercalation into a Spinel Oxide Host. *Adv. Mater.* **2015**, *27*, 3377-3384.

(44) Yuan, C.; Zhang, Y.; Pan, Y.; Liu, X.; Wang, G.; Cao, D. Investigation of the Intercalation of Polyvalent Cations (Mg^{2+}, Zn^{2+}) into λ-MnO_2 for Rechargeable Aqueous Battery. *Electrochim. Acta* **2014**, *116*, 404-412.

(45) Gregory, T. D.; Hoffman, R. J.; Winterton, R. C. Nonaqueous Electrochemistry of Magnesium Applications to Energy Storage. *J. Electrochem. Soc.* **1990**, *137*, 775-780.

(46) Muldoon, J.; Bucur, C. B.; Gregory, T. Quest for Nonaqueous Multivalent Secondary Batteries: Magnesium and Beyond. *Chem. Rev.* **2014**, *114*, 11683-11720.

(47) Wang, L.; Li, Y. H.; Han, Z. D.; Chen, L.; Qian, B.; Jiang, X. F.; Pinto, J.; Yang, G. Composite Structure and Properties of Mn_3O_4/Graphene Oxide and Mn_3O_4/Graphene. *J. Mater. Chem. A* **2013**, *1*, 8385-8397.

(48) Montes, J. M.; Cuevas, F. G.; Cintas, J.; Urban, P. Electrical Conductivity of Metal Powders under Pressure. *Appl. Phys. A* **2011**, *105*, 935-947.

(49) Lei, S.; Tang, K.; Fang, Z.; Zheng, H. Ultrasonic-Assisted Synthesis of Colloidal Mn_3O_4 Nanoparticles at Normal Temperature and Pressure. *Cryst. Growth Des.* **2006**, *6*, 1757-1760.

(50) Suslick, K. S.; Cichowlas, A. A.; Grinstaff, M. W. Sonochemical Synthesis of Amorphous Iron. *Nature* **1991**, *353*, 414-416.

(51) Didenko, Y. T.; McNamara, W. B.; Suslick, K. S. Hot Spot Conditions during Cavitation in Water. *J. Am. Chem. Soc.* **1999**, *121*, 5817-5818.

(52) Wang, L.; Chen, L.; Li, Y. H.; Ji, H. M.; Yang, G. Preparation of Mn_3O_4 Nanoparticles at Room Condition for Supercapacitor Application. *Powder Technol.* **2013**, *235*, 76–81.

(53) NuLi, Y.; Zheng, Y.; Wang, Y.; Yang, J.; Wang, J. Electrochemical Intercalation of Mg^{2+} in 3D Hierarchically Porous Magnesium Cobalt Silicate and Its Application as an Advanced Cathode Material in Rechargeable Magnesium Batteries. *J. Mater. Chem.* **2011**, *21*, 12437-12443.

(54) Arthur, T. S.; Zhang, R.; Ling, C.; Glans, P. A.; Fan, X.; Guo, J.; Mizuno, F. Understanding the Electrochemical Mechanism of K-αMnO_2 for Magnesium Battery Cathodes. *ACS Appl. Mater. Interfaces* **2014**, *6*, 7004-7008.

(55) Ling, C.; Zhang, R.; Arthur, T. S.; Mizuno, F. How General is the Conversion Reaction in Mg Battery Cathode: A Case Study of the Magnesiation of α-MnO_2. *Chem. Mater.* **2015**, *27*, 5799-5807.

(56) Okamoto, S.; Ichitsubo, T.; Kawaguchi, T.; Kumagai, Y.; Oba, F.; Yagi, S.; Shimokawa, K.; Goto, N.; Doi, T.; Matsubara, E. Intercalation and Push-Out Process with Spinel-to-Rocksalt Transition on Mg Insertion into Spinel Oxides in Magnesium Batteries. *Adv. Sci.* **2015**, *2*, 1500072-1500081.

(57) Shterenberg, I.; Salama, M.; Gofer, Y.; Levi, E.; Aurbach, D. The Challenge of Developing Rechargeable Magnesium Batteries. *MRS Bull.* **2014**, *39*, 453-460.

(58) Aurbach, D.; Schechter, A.; Moshkovich, M.; Cohen, Y. On the Mechanisms of Reversible Magnesium Deposition Processes. *J. Electrochem. Soc.* **2001**, *148*, A1004-A1014.

(59) Saha, P.; Jampani, P. H.; Datta, M. K.; Okoli, C. U.; Manivannan, A.; Kumta, P. N. A Convenient Approach to Mo_6S_8 Chevrel Phase Cathode for Rechargeable Magnesium Battery. *J. Electrochem. Soc.* **2014**, *161*, A593-A598.

(60) Kim, J. S.; Chang, W. S.; Kim, R. H.; Kim, D. Y.; Han, D. W.; Lee, K. H.; Lee, S. S.; Doo, S. G. High-Capacity Nanostructured Manganese Dioxide Cathode for Rechargeable Magnesium Ion Batteries. *J. Power Sources* **2015**, *273*, 210-215.

(61) Feng, Z. Z.; Yang, J.; NuLi, Y. N.; Wang, J. L. Sol-Gel Synthesis of $Mg_{1.03}Mn_{0.97}SiO_4$ and Its Electrochemical Intercalation Behavior. *J. Power Sources* **2008**, *184*, 604-609.

(62) Jiao, L. F.; Yuan, H. T.; Si, Y. C.; Wang, Y. J.; Wang, Y. M. Synthesis of $Cu_{0.1}$-Doped Vanadium Oxide Nanotubes and Their Application as Cathode Materials for Rechargeable Magnesium Batteries. *Electrochem. Commun.* **2006**, *8*, 1041-1044.

(63) Liu, Y.; Jiao, L.; Wu, Q.; Zhao, Y.; Cao, K.; Liu, H.; Wang, Y.; Yuan, H. Synthesis of RGO-Supported Layered MoS_2 for High-Performance Rechargeable Mg Batteries. *Nanoscale* **2013**, *5*, 9562-9567.

Table of Contents artwork